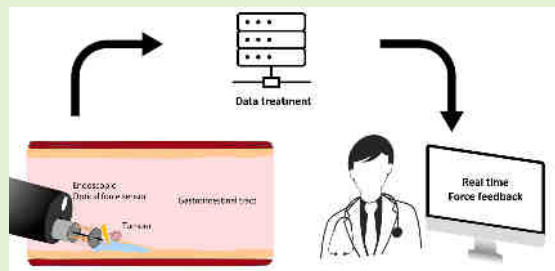


# Tri-Axial Force Sensor in a Soft Catheter Using Fiber Bragg Gratings for Endoscopic Submucosal Dissection

Ramzi Ben Hassen, Arnaud Lemmers, Alain Delchambre

**Abstract**—Endoscopic Submucosal Dissection (ESD) is an advanced endoscopic technique with renowned clinical benefits but still a challenging procedure. The lack of force-feedback leading to insufficient or excessive contact force between the tip of the knife and the tissue, i.e ineffective treatment or dangerous perforation, makes ESD requiring a high level of expertise and dexterity to master it, especially for trainees. In this paper, we propose to enhance the training in ESD by integrating Fiber Bragg Gratings (FBGs) as 3 degrees-of-freedom optical force sensors into the polymer catheter of the electrosurgical knife aiming to measure  $F_x$ ,  $F_y$  and  $F_z$ . 3 FBGs are placed circumferentially to the section of the catheter using nitinol tubes and a 2-point pasting method. A force calibration test bench was specifically designed to calibrate the force sensor in 30 3D spatial directions that cover most of its use cases. Non-linear regression models were implemented to tackle the non-linearities between the wavelength shifts of the FBGs and the forces applied, inherent to prototyping errors and non-linearity of the soft material. A hybrid model made of mono- and bi-layered neural networks for the prediction of  $F_x$  and  $F_y$  and a support vector regression for the prediction of  $F_z$  was built and showed root-mean-square error (RMSE) along transverse directions (XY) less than 3% of the full scale [-500; 500] mN and RMSE less than 10% along the axial direction (Z). These models were also verified in dynamic conditions. The results are promising and satisfying all the technical requirements.



**Index Terms**—Endoscopic Submucosal Dissection (ESD), Fiber Bragg Gratings (FBGs), Force sensor, Force calibration, Regression model, Therapeutic endoscopy, Training in ESD.

## I. INTRODUCTION

### A. Motivation

**T**HERAPEUTIC endoscopy using long, thin and flexible endoscopes enables the treatment of multiples digestive tract disorders by the mean of advanced endoscopic techniques [1]–[3]. This allows the development of very low invasive procedures that reduce patients burden and shorten stays in hospitals, not mentioning the fact that it enables also less morbidity and mortality compared to the surgical approach. One of these therapeutic procedures is the endoscopic submucosal dissection (ESD).

This work was supported by Fonds de la Recherche Scientifique (FRS-FNRS) through a research project (PDR grant T.0251.18), by David and Alice Van Buuren Fund, by Jaumotte-Demoulin and by Michel Cremer Foundations.

Ramzi Ben Hassen is with Bio-, Electro- and Mechanical- Systems (BEAMS), Ecole polytechnique de Bruxelles, Université libre de Bruxelles, Brussels, Belgium. (e-mail: rbenhass@ulb.be).

Arnaud Lemmers is with Department of Gastroenterology, Hepatopancreatology and Digestive Oncology, CUB Erasme Hospital, Université Libre de Bruxelles (ULB), Brussels, Belgium (e-mail: arnaud.lemmers@hubruxelles.be).

Alain Delchambre is with Bio-, Electro- and Mechanical- Systems (BEAMS), Ecole polytechnique de Bruxelles, Université libre de Bruxelles, Brussels, Belgium (e-mail: adelch@ulb.be).

ESD enables the *en bloc* complete resection of gastrointestinal tumors regardless of their size or location. Moreover, compared to the more traditional endoscopic mucosal resection (EMR), ESD shows a lower recurrence rate and a better histopathological assessment to determine whether the treatment was curative or not [3]. It is performed by several tools passing through the working channel of an endoscope and consists in firstly delineating the margins of the lesion using cautery (A on figure 1a). Then, in order to elevate the lesion from the underlying muscular layers and allow safety margins for the followings steps, a lifting agent (mostly colloid solution (i.e glycerol) or saline) is injected into the submucosa (B). The mucosa of the tumor is subsequently cut circumferentially using an electrosurgical knife (C). Finally, the submucosa beneath the lesion is dissected in a free-hand manner until the target tumor is completely resected (D-F) [6]. The endoscopic view of ESD is illustrated in figure 1b.

Since its first application in Japan, ESD has rapidly grown in Southeast Asia where expertise was easily found. Hence, there is a lack of diffusion and adoption of ESD in Western countries despite a huge amount of publications on this topic. Several reasons can be listed to explain it and can be grouped in three major sets that are (i) the lack of understanding of the clinical benefits of ESD, (ii) the lack of training methodology

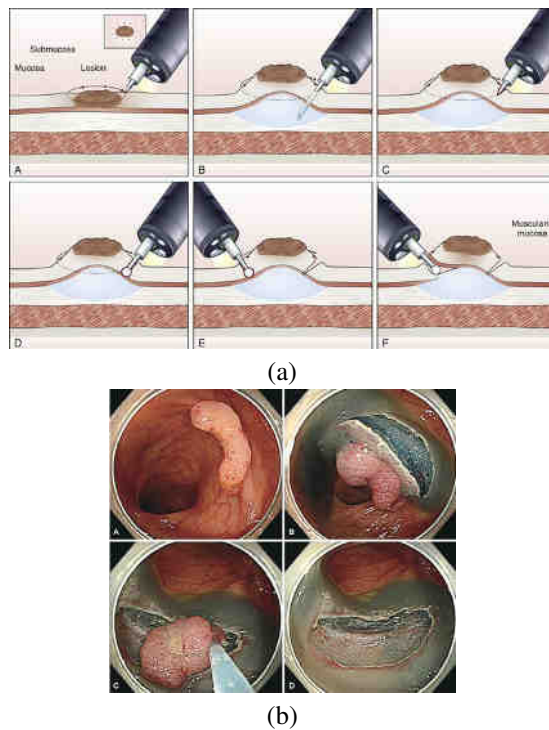


Fig. 1: (a) Steps of ESD [4]. (b) Endoscopic view of ESD [5].

and expertise centers (iii) and the technically demanding skills required to perform the procedure. The latter is a major challenge of ESD because a high level of training and dexterity is needed to safely perform it and prevent longer procedure time and complications, mainly perforation and bleedings [3], [7]–[9].

### B. Related technical solutions

Several technical solutions to help physicians master ESD have been provided in the literature. One of the causes that complicates the procedure is the lack of bimanual dexterity due to the endoscopic framework in particular during the dissection phase where it would be useful to maintain the dissected tissue in traction in order to complete the resection so it doesn't hang down over the working field. In 2018, [10] developed a robotic system called ESD Cyclops. The design consists on a robotic surgical attachment composed of a deployable scaffold and two arms that can be mounted on the end of any flexible endoscope. Another attempt to resolve the tissue traction difficulty and avoid blind dissection of the mucosa is brought by [11] and relies on a suture pulley countertraction method. Other studies suggested to gain visualization during ESD by using a magnetic anchored-guided procedure (MAG-ESD) for gastric [12] and colorectal lesions [13]. After marking the lesion and beginning the incision of the mucosa, the principle is to place a neodymium magnet on the edge of the lesion by the use of a hemoclip. An external magnet is maneuvered with an arm to offer proper counter traction in function of endoscopist needs. Multi-task robotic endoscopy platforms have also blossomed such as the EndoSamurai (Olympus, Japan) [14], the MASTER (EndoMaster, Singapore), ISIS-

Scope/STRAS system, the Scorpion shaped robot [15], the RAFF (robotic-assisted flexible endoscope) [16] among others [14], [17]. A recent work developing a snake-like flexible robot [18] aiming to be flexible enough for easy insertion and to maintain a rigid shape to transmit the forces applied on instrumentation still need to demonstrate its ability during ESD surgeries. Most of these technical solutions were primarily focused on providing tissue counter traction during dissection phase, gaining bimanual dexterity or maneuverability. Hence, these propositions have never been adopted widely and in clinical daily practice. The bulkiness of robotic platform as well as the mechanical- or magnetic-based counter traction methods have complicated ESD with new steps such as the anchoring of magnets or suturing that added new learning curves. Robotic devices on the other hand extended the number of operators and didn't demonstrate a clear usability to ESD.

### C. FBG force sensor

The lack of force feedback during the procedure might play a significant role in its slow adoption and in particular during training. This is specific to most of endoscopic procedures because the tools to operate used by the physician passes through the working channel of the endoscope which is relatively long (up to more than 1 meter) and induces friction forces which make the useful forces, i.e. the interaction forces between the tip of the tool and the tissue to treat, completely drowned and lead to a loss of haptic information to the physician. This might be critical for ESD where the adverse events such as perforations are likely to happen. A force feedback system would be relevant to flatten the learning curve of ESD by helping trainees adjust the right amount of force during the procedure (not too high to avoid perforation but sufficiently to have an effect on tissue) and make it more accessible and safer. This system should be directly integrated to the electro-surgical knife in order to avoid bringing the disadvantages mentioned before, namely the adding of new steps to ESD protocol and the augmentation of operators.

Fiber Bragg Gratings (FBGs) are particularly fitted to fulfill the force sensing function because of their intrinsic properties of flexibility, high sensitivity, biocompatibility (according to ISO 10993 [19]), chemical inertness, robustness to electromagnetic interference as well as their small size that make them very appropriate for the development of force sensing medical devices.

Prior work has been implementing FBG as force sensors for surgical instruments or endoscopic devices. In the field of cardiac procedures, Li et al. [20] designed an ablation catheter with an FBG sensor composed of 5 fibers and a force-sensitive flexure in an aluminum alloy (typical hinge design) able to sense the forces in 3 directions. For the same application, Gao et al. [32] developed a 3 DOF force sensor using 4 FBGs. They used a deformable structure with parallel flexural hinges to have a good balance between axial (low) and transverse (high) stiffness. He et al. proposed for vitreoretinal surgery [31] a high resolution submillimetric 3 DOF force sensing pick instrument using 4 FBGs. Deng et al. [21] implemented also 4 FBGs in a miniature triaxial force

sensor integrated at the tip of a flexible ureteroscope designed with a notched flexure of multilayer continuous beams to avoid the crosstalk between axial and lateral forces. Ping et al. [22] proposed a miniaturized flexible instrument based on contact-aided compliant mechanisms and FBG sensing for intraoperative gastric endomicroscopy implementing 3 FBGs equally distributed on the circumference of the catheter for transverse force sensing and one off-centre FBG for axial force measurements, allowing the space for a central hollow for the probe. Similarly, Wu et al. developed a 3 DOF force sensor using 3 FBGs in the field of robotic bronchoscopy, in particular optical biopsy using probe-based confocal laser endomicroscopy (pCLE) [33] using only 3 FBGs for 3 DOF sensing. Lai et al. [23] developed a standalone tri-axial force sensor that can be seamlessly integrated into an endoscopic robotic arm to measure pulling and lateral forces. 3 FBGs are embedded in the sensing structure, where one is located at the center hole of the structure (diameter 1.4 mm), and the other two are eccentrically placed around the structure. Although these studies provided force sensing devices using FBGs, most of them have structures and hinges difficult to fabricate or the FBGs are exposed to environment, which is not suitable for endoscopic application and moreover those devices are made of rigid material with limited flexibility.

#### D. Paper contributions and structure

As mentioned in the previous section, several limitations can be encountered when implementing FBGs as a force sensor, such as dimensional bulkiness and complex design. In this paper, we propose a triaxial force sensor in the catheter of an electrosurgical knife using FBGs to flatten the learning curve of ESD, which to the best of the author's knowledge has not yet been achieved. The proposed sensor is designed to be 1) simple with no notch or complex mechanical structure, 2) easily fabricated by accommodating the FBGs in a soft material substrate obtained by simple extrusion, while 3) enabling 3 DOF force sensing using only 3 FBGs thanks to a hybrid machine learning model. These 3 features are the main contributions of this work.

The rest of the paper is structured as follows: Section II covers the design of the sensor from the theoretical aspect of FBG and technical requirements to prototyping and force calculation method. Section III presents the experimental setup and protocol for force calibration of the sensor. Section IV is related to the results of the calibration and how non-linearities are dealt with using a hybrid machine learning model along with the performance evaluation of the force sensor. Finally, a discussion of this work and future improvements is given in Sections V and VI.

## II. DESIGN OF THE SENSOR

### A. Requirements

An electrosurgical knife is mainly composed of two parts : a catheter made of soft polymer and a conductive wire that is literally responsible of the electrocautery. The latter is embedded inside the catheter. Several options are possible on the manner to integrate FBGs in an electrosurgical knife

<b>Dimensions</b>	FSD diameter	< 2.8 mm
	FSD length	≥ 1600 mm
<b>Sensing performance</b>	Range of forces	[-500;500] mN for $F_x$ and $F_y$ [0;500] mN for $F_z$
	Resolution	5 mN

TABLE I: Main requirements for the design of the FSD.

to measure the tool's interaction forces at its tip: directly implementing the gratings on the conductive wire or on the catheter or a combination of both. The best configuration is inspired by a patent filled by Université libre de Bruxelles (US10022190B2) and depicted in figure 2. The FBGs are equally distributed distally on the circumference of the catheter in their peripheral respective lumen and a central hollow is meant to host the conductive wire of the electrosurgical knife. This design allows to avoid prototyping or manufacturing a new conductive wire with grooves to host the FBGs with no guarantee that it would not heavily impact the electrocautery itself and thus the safety of ESD. **From now on, the device to develop is then a catheter with integrated FBGs and will be called force sensing device (FSD).**

The geometry of the FSD should fit the diameter of the endoscope's working channel which is usually 2.8 mm. As for its length, it needs to be greater than 1600 mm which is the minimum length of the working channel.

The number of DOF should be three since ESD is performed in 3 spatial directions : laterally, up and down and along the axis of the tool during both incision and dissection phases.

To the authors knowledge, no data in the literature provide the amount of force exerted during an ESD. However, some studies [22], [24], [33] give an indication of the average contact forces during a classic colonoscopy or an endomicroscopy which are in the range of 0-600 mN. Therefore, for the purpose of this work, the range of forces expected to measure will be defined by default between -500 mN and 500 mN for the transverse forces  $F_x$  and  $F_y$  and between 0 and 500 mN for the axial one  $F_z$ . The resolution expected for that range of force would be 5 mN, i.e. maximum 1% of the full scale.

The main requirements are summarized in table I.

### B. Structure and working principles

1) *FBG sensing mechanism*: The sensing mechanism of FBG is well known and has been used in a very diverse range of applications. The working principle is shown in Figure 3. When light propagates through the fiber, the periodic perturbation of the refractive index along a certain length of the fiber, called the Bragg grating, reflects the Bragg wavelength. The latter is influenced by strain and temperature applied to the grating [28].

The sensitivity to strain and temperature is described by the following equation 1:

$$\lambda_B = 2n_{eff}\Lambda, \quad (1)$$

where  $\lambda_B$  is the Bragg wavelength,  $n_{eff}$  the effective refractive index and  $\Lambda$  the period of the grating. Typical lengths of uniform gratings vary from 1 mm to 10 mm. The temperature

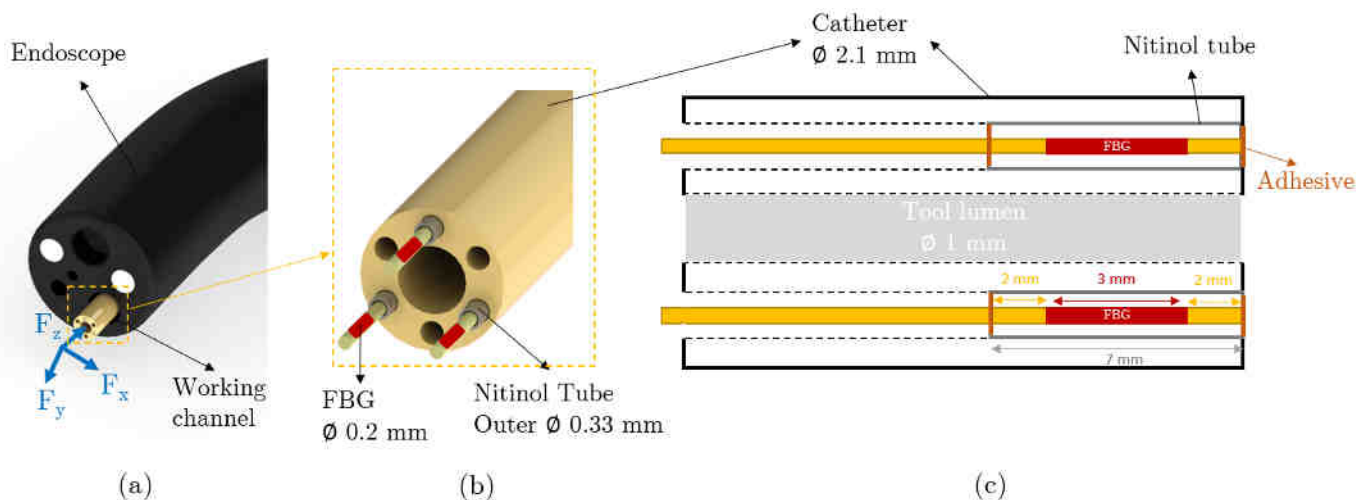


Fig. 2: CAD model of the force sensing device (a) illustration of the FSD in the working channel of an endoscope (b) exploded view of the close up (c) section view of the distal force sensing part.

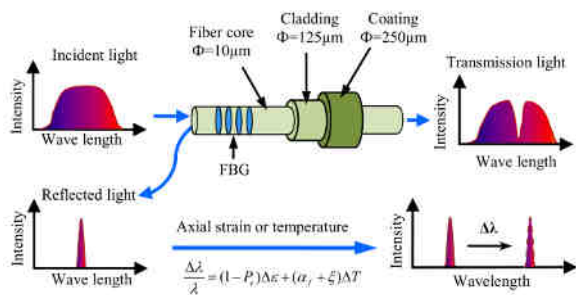


Fig. 3: Principle of Fiber Bragg Grating [28].

affects  $\lambda_B$  through the thermal expansion and the thermo-optic effect while the strain influences the Bragg wavelength by changing the grating's period and due to elastic-optic effect [29]. The shift in Bragg wavelength can be described by equation 2 :

$$\Delta\lambda_B/\lambda_B = (\alpha + \xi) \cdot \Delta T + (1 - P_e) \cdot \Delta\epsilon, \quad (2)$$

where  $\Delta T$ ,  $\Delta\epsilon$  are the variation in temperature and strain respectively,  $\alpha$  the thermal expansion coefficient ( $C^{-1}$ ),  $\xi$  the thermo-optic coefficient ( $C^{-1}$ ) and  $P_e$  the elasto-optical coefficient. The coefficients are considered constant. Giving equation 2, the temperature and the strain can be measured by detecting the center wavelength of the reflected spectrum. This cross-sensitivity makes the use of FBGs for only strain or force sensing a challenge because of the need to decouple the temperature's influence. Moreover, a calibration process is crucial to compute a relationship between the wavelength shifts caused by strain and the applied force in its three components.

2) *Components*: The device is made of three main parts : a soft polymer catheter, optical fibers with inscribed FBGs and nitinol tubes. The first is designed in a way to allow a central lumen to place the electrosurgical tool and several peripheral multilumen to host the optical fibers. It has been manufactured

by Transluminal (France) according to our requirements. To control the adhesion process of the fiber to the catheter using cyanoacrylate (Loctite) and avoid introducing high non-linearities for the strain transfer from the tip of the catheter to the FBG itself, nitinol tubes (Johnson Matthey, USA) are used to enable a two-point pasting method as described by [25], [26] who suggested that gluing the FBG at its two ends only enables to apply a pretension which allows direct compression and stretching along its axial direction and improves sensitivity and resolution while avoiding chirping failure. This method allows the grating itself to be clear from any adhesive. The FBGs are coated with polyimide and manufactured by AtGrating (China) using the phase mask method. Their length is chosen to be 3 mm. Although long gratings have a higher signal-to-noise ratio, the shorter the FBG the better stability against strain gradients [27]. Therefore, 3 mm seems to be a good trade-off length which has already been implemented in similar work [31], [33] with very satisfactory results in terms of force resolution. The properties of the FBGs are listed in table II.

Properties	FBG1	FBG2	FBG3
Bragg Wavelength	1550.104 nm	1554.918 nm	1559.857 nm
Bandwidth	0.564 nm	0.529 nm	0.535 nm
Reflectivity	70.14%	66.50%	70.14%

TABLE II: Optical properties of the FBGs used in the FSD. They all are 3 mm long.

Table III summarizes the materials properties of the components of the FSD.

### C. Prototyping and assembly

The first step illustrated in figure 5a consists in cutting the fiber and the nitinol tube according to the dimensions mentioned in figure 2. Because the nitinol tube has an outer diameter close to the inner diameter of the catheter's lumen and thus to avoid too much friction in the insertion phase,

Component	Material	Young's Modulus
Optical fiber	SiO <sub>2</sub> + polyimide coating	Around 16.56 GPa
Catheter	Pebax 7233 SA 01 MED	510 MPa
Tubes	Nitinol	28 to 41 GPa
Adhesive	Cyanoacrylate	/

TABLE III: Materials used in the FSD.

the bare fiber is primarily inserted into the catheter before attaching it to the nitinol tube. Once this step realized, the fiber passes through the nitinol tube until its distal tip reaches the end of the latter where the first point pasting using cyanoacrylate (Loctite) is applied. Afterwards, the whole is placed on a pretension bench. A tension is applied and monitored with a software to evaluate the effect on the wavelength shift of the FBG. The second point pasting is performed on the other end of the nitinol tube. Several software checks are done to verify that the tension is still applied even after release of the fiber. Once the tension on all the fibers was implemented (see figure 5b), a pure mechanical insertion of the nitinol tube inside the catheter was conducted. The friction is sufficiently high to not require the use of glue to secure the whole assembly. The final prototype is illustrated in figure 5c. The flow chart of the prototyping and assembly process is described in figure 4.

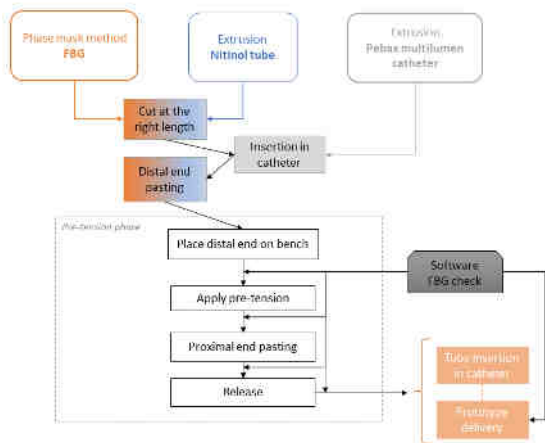
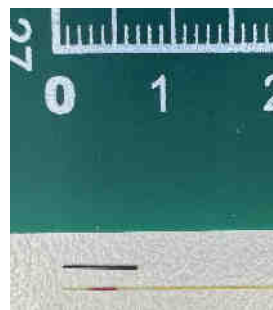


Fig. 4: Prototyping flow chart which is applied for each FBG.

#### D. Force calculation method

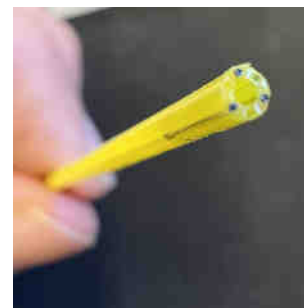
Due to non-linearities that are introduced because of imprecisions in manufacturing and FBGs installation on the sensor, mathematical model can be quite limiting in describing the device behavior when external forces are operating on it. Furthermore, the more complex they get, the more computational efficiency they lose. In fact, the resolution of the inverse matrix  $K$  (see equation 3) describing the relationship between wavelength shift and measurand (strain and temperature) can become quite demanding when the device is geometrically sophisticated [30].



(a) The black tube is made of nitinol and is cut at a length of 7 mm. The FBG is represented by the red mark on the yellow optical fiber.



(b) The fibers are pretensioned and the FBGs are inside the nitinol tubes.



(c) Capture of the FSD made of 3 FBGs encapsulated inside nitinol tubes inserted into the multi-lumen catheter.

Fig. 5: Assembly process of the FSD.

$$\Delta F = K \cdot \Delta \lambda \quad (3)$$

A first attempt to overcome this limitation was proposed in [31] by using Bernstein polynomials as fitting method. Other approaches in [32] and [33] consisted in applying support vector regression to provide a model of 3 DOF force prediction based on a supervised learning while an artificial neural network has been used for the same purpose in [34] and [30]. The challenge when using such algorithms is to choose the right one, which needs several tests, and to accept to often operate with a black box.

In this work, a data driven method has been implemented to decouple the three components of the force  $F_x$ ,  $F_y$  and  $F_z$  based on the wavelength shifts of the FBGs only. A hybrid supervised learning model using feedforward neural networks (NNs) to calculate the transverse forces and support vector

regression (SVR) with a gaussian kernel to compute the axial compression force was trained and validated by K-fold cross validation. The procedure that led to this regression model can be summarized in the three steps as shown below :

- 1) Collect calibration data for training and testing;
- 2) Compare performance of NNs and SVR for each component of the force (by selecting the best hyperparameters using Bayesian optimization and grid search method);
- 3) Apply the cross validation method to evaluate the performance of the selected supervised learning algorithm.

The study is conducted on the regression learner app of Matlab where a lot of features are available including data exploration, automated training and methods to optimize hyperparameters, among others.

### III. CALIBRATION

#### A. Introduction

To be able to perform force sensing, a calibration of the FSD is necessary to find a relationship between the wavelength shifts and the forces applied on the tip of the device that generate the latter in several spatial configurations that cover mostly all the use cases of ESD.

#### B. Test bench

A specific test bench has been designed to achieve a 3 DOF calibration to build a data based model of the wavelength shifts-force relation. Figures 6 and 7 illustrate this test bench. It is composed of several elements :

- an FBG interrogator (FBGS FBG 804D) to record the optical responses of the FBGs and translate them to wavelength shifts ;
- an analytical scale (Radwag, precision 0.1 g) to measure the force applied on the tip of the prototype;
- a 1 DOF motorized linear stage with its controller (Thorlabs);
- a 2 DOF manual rotary stages with a yaw- $\beta$  and roll- $\alpha$  angles allowing to represent a coordinate system explained in the next section (III-C). The whole is assembled using 3D printed parts allowing the combined rotation of both yawing and rolling angles.
- the prototype to calibrate fixed in a clamp able to rotate along its longitudinal axis;
- a labview interface designed to receive simultaneously the information of wavelength shifts and weight readings from the interrogator and the scale while being able to record the data during the calibration by saving them into a text file.

#### C. Protocol

The calibration of the prototype consists in collecting a large amount of training data to feed a regression model in order to obtain the relationship between the forces acting on the tip of the prototype and the wavelength shifts. For that purpose, rolling and yawing angles  $\alpha$  and  $\beta$  (see figure 9) are defined along with a parameter  $d$  representing the forward



Fig. 6: Experimental setup for the data collection of the force sensor during calibration.

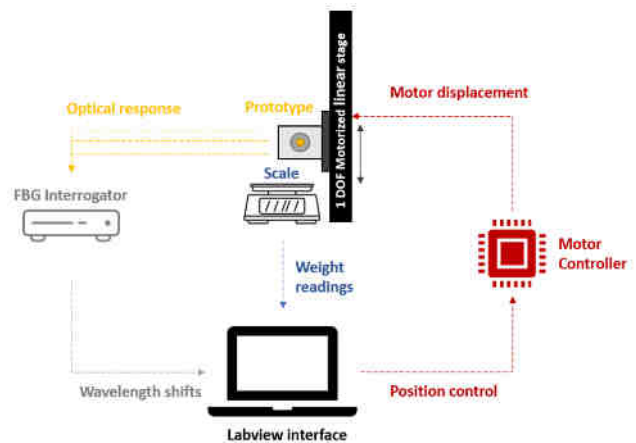


Fig. 7: Block diagram of the calibration test bench highlighting the data flow.

and backward distance traveled by the linear stage to build a 3 DOF coordinate system able to derive the three components of the force as follows :

$$F_x = F \cos \alpha \cos \beta \quad (4)$$

$$F_y = F \sin \alpha \cos \beta \quad (5)$$

$$F_z = F \sin \beta \quad (6)$$

The first task is to define the values of  $\alpha$  and  $\beta$  according to the use cases of the FSD in endoscopic settings. Figure 8 illustrates a typical random orientation of an electrosurgical knife during ESD. After analyzing several procedures, the  $\beta$  angle varies in the range  $]0^\circ;90^\circ[$ . The limit angles are excluded. Indeed, with  $\beta = 0^\circ$  the knife is in parallel to the tissue to cut which doesn't allow to penetrate it while when  $\beta = 90^\circ$  the tool is perpendicular to the tissue which is very dangerous since perforation is most likely to happen in that configuration. For the calibration purpose, the values of  $\beta$  considered are ranged from  $0^\circ$  to  $90^\circ$  with a step of  $15^\circ$  (extreme values are included even if they're not commonly used in ESD but here the goal is to ensure the ability of the FSD to measure forces even in the limits). The value of the

step is chosen as a trade-off to explore a sufficient number of  $\beta$  angles without overwhelming the calibration procedure. Concerning the  $\alpha$  angle, ESD doesn't constrain its values. Practically, the physician positions the tool in a given  $\alpha$  angle and proceeds to the cutting and the dissection. This angle may vary during the procedure. For the purpose of this thesis, the range for the  $\alpha$  angle corresponds to up/down and left/right movements (XY plane) :  $0^\circ$ ,  $90^\circ$ ,  $180^\circ$  and  $270^\circ$ . In this way, the transverse forces  $F_x$  and  $F_y$  are canceled alternately. This will allow to verify the ability for the FSD to decouple the force components. Considering these ranges, the combination of  $\alpha$ - $\beta$  angles generates 28 directions.



Fig. 8: Left: endoscopic footage of an ESD. Right: Schematic image of ESD [35].  $\alpha$  and  $\beta$  angles are highlighted in a typical random orientation during an ESD procedure.

For each direction, i.e. couple of yawing and rolling angles, the tip of the prototype is brought forward and backward against the scale using the motorized linear stage. The applied weight ranged from 0 g to 50 g (increments/decrements with a step of 5 g) to obtain a force magnitude ranging from 0 to 500 mN for  $F_z$  and -500 to 500 mN for  $F_x$  and  $F_y$ . This was applied three times for each direction to evaluate the repeatability of the sensor and of the FBGs specifically.

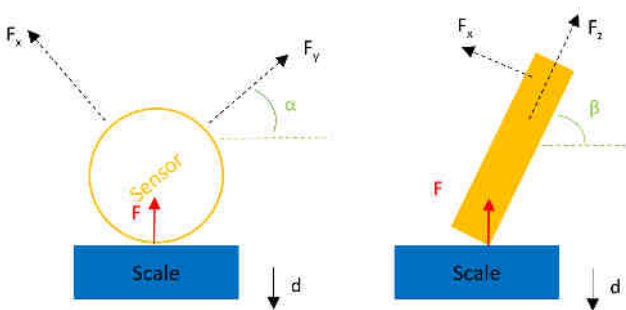


Fig. 9: Definition of the rolling and yawing angles  $\alpha$  and  $\beta$ . Left (XY plane): section view of the prototype with  $\beta = 0$ . Right (XZ plane): longitudinal view of the prototype with a given yawing elevation.

## IV. RESULTS

### A. Non-linearity

Most of the shifts-weight relationships recorded during the calibration process showed high non-linearity and hysteresis.

Indeed, the prototype imperfections as well as the influence of viscoelastic effects due to the polymer which the catheter is made of and the adhesive used to secure the FBGs inside the nitinol tubes introduce these non-linear behavior as it is illustrated in figure 10 for one group of experimental data where  $\alpha = 180^\circ$  and  $\beta = 15^\circ$ . This type of calibration data will require the use of non-linear regression models for the prediction of the force along XYZ directions.

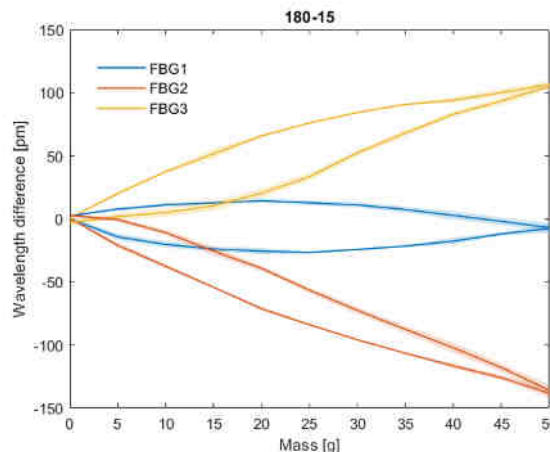


Fig. 10: One group of experimental data ( $\alpha = 180^\circ$  and  $\beta = 15^\circ$ ) where the straight line represents the mean of the wavelength shifts from the three loading/unloading cycles and the shaded area its standard deviation.

### B. Repeatability

To evaluate the consistency of the force sensor response, a repeatability examination has been performed. The calibration data are made of 1980 samples where one sample corresponds to one wavelength shift in function of the weight applied against the scale (for instance 40 pm at 30 g during load phase). Within the total number of samples, three repetitions were conducted. The whole is divided into subsets where each subset is composed of wavelength shifts measured with the same calibration direction ( $\alpha$ - $\beta$ ) and magnitude (scale readings), generating  $1980/3=660$  subsets in total. The mean and the standard deviation are computed for each subset, the latter being a measure of the repeatability. All standard deviations are combined per FBG to provide a **repeatability of 1.82 pm, 2.01 pm and 2.53 pm for FBG1, FBG2 and FBG3 respectively**. Knowing that the interrogator has a wavelength repeatability of 1 pm and a wavelength stability ranges between 2 and 5 pm [31], the FSD demonstrates a reliable repeatability consistent with the intrinsic optical properties of the interrogator.

### C. Force prediction

The non-linear regression models were trained with the input calibration data using only the wavelength shifts of FBG1, FBG2 and FBG3 as predictors. After following the method described in section II-D, the models that were chosen

using K-fold cross validation (K=5) are listed in table IV along with their optimized hyperparameters. The root-mean-square error (RMSE) obtained for the prediction of the three components of the force  $F_x$ ,  $F_y$  and  $F_z$  are also reported. The performance are quite similar regarding the transverse forces  $F_x$  and  $F_y$ . The RMSE is less than 3% of the full scale (f.s.) which ranges from -500 to 500 mN. The prediction of the axial force  $F_z$  is less accurate with an RMSE reaching almost 10% of the f.s. ranging from 0 to 500 mN.

Force	Model	Settings
$F_x$	NN	Number of layers = 1 Size of layers = 400 nodes
$F_y$	NN	Number of layers = 2 Size of layers = 200 and 100 nodes
$F_z$	SVR	C = 1.2 $\epsilon$ = 0.0183 Kernel scale = 0.47

**TABLE IV:** Summary of the models trained to predict  $F_x$ ,  $F_y$  and  $F_z$ . The values reported are computed when the models are applied to the training data and validated by 5 folds cross validation.

Figures 11 (a) and (d) show that there is a very satisfying correlation between predicted and actual values for the transverse forces (respectively  $R^2$  equal to 0.96 and 0.98). Residual errors concerning the prediction of  $F_x$ , i.e. the difference between actual and predicted values, are also calculated to evaluate the accuracy of the model on the training data set (see figure 11 (c)). The mean error is 0.04 +/- 20.3 mN. It appears that most of the residual error stays within +/- 50 mN which is very satisfying knowing that the global RMSE error is equal to 29.8 mN. This observation is even stronger for  $F_y$  where the histogram is narrower around 0 mN (figure 11). The mean error is 0.05 +/- 13.4 mN. Most of the residual errors remain within +/- 25 mN which is slightly better than the performance of the model predicting  $F_x$  but it still stays in the same order of magnitude (just like the RMSE). Figures 11 (b) and (e) illustrate that there is a low dependence of the residual error to most of the actual force values with a noticeable exception around 0 mN. The prediction of zero values for  $F_y$  is however better than what is observed for  $F_x$ .

The SVR model for the prediction of the axial force  $F_z$  provides an RMSE of 49.9 mN representing 9.9 % of the full scale with a value for  $R^2$  equal to 0.87. The difference of RMSE compared to the models predicting  $F_x$  and  $F_z$  is clearly noticeable. In fact, it was expected that the prediction of compression forces performs worse compared to the transverse forces as it is even the case in the literature [32], [33]. One explanation can be that the imperfections of the prototype such as the non-planar section generates shear forces that cross talk with the pure compression force. The viscoelastic deformation of the soft polymer might also be a reason behind this lower prediction capability of the force  $F_z$  on the training data. Since  $F_z$  is calculated based on equation 6, the lower the value of  $\beta$ , the lower the magnitude of  $F_z$ . It appears on the graph in figures 12 (a) and (b) that for low values of  $\beta$  the residual error

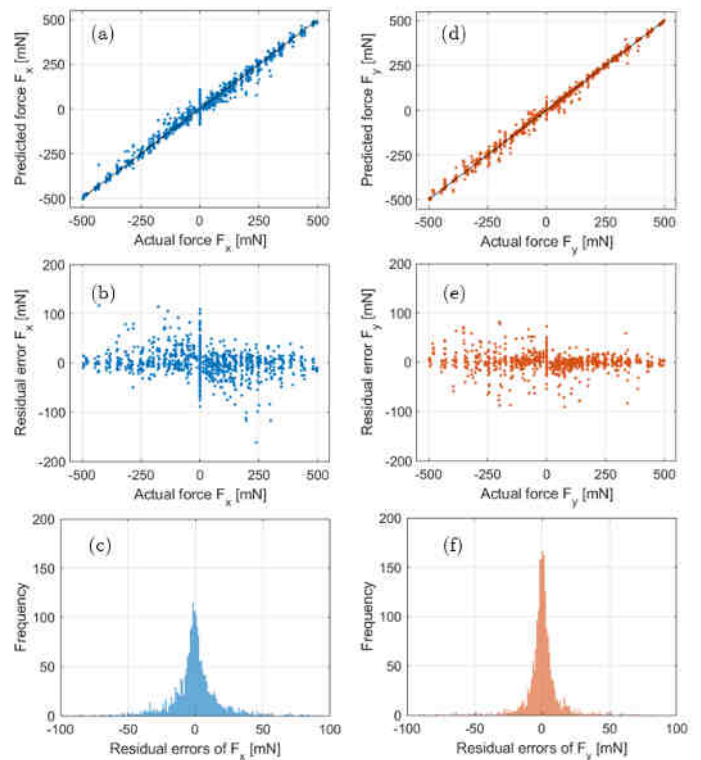


**Fig. 11:** The predicted transverse force  $F_x$  versus the actual value using (a) neural networks, (b) its residual error, and (c) the histogram of the residual error of  $F_x$ . (d) The predicted transverse force  $F_y$  versus the actual value using neural networks, (e) its residual error, and (f) the histogram of the residual error of  $F_y$ .

is greater. It can be explained by the fact that the lower  $\beta$  is, the higher the transverse forces are (see equations 4 and 5) that can cross talk with the compression force. The histogram of the residual errors on the training data set are showed in figure 12 (c). The mean error is 2.2 +/- 37 mN. The dispersion is clearly higher compared to previous models. Despite the fact that most of the residual error stays within +/- 50 mN, the distribution is more flat around 0 mN with two peaks probably resulting from the black box internal operations of the SVR model.

Knowing that the resolution of the interrogator is 1 pm, one can derive the resolution of the FSD by taking the force range divided by the smallest FBG wavelength shift range in the calibration data for the three components of the force. The results are 5.3 mN, 5.4 mN and 2.9 mN for  $F_x$ ,  $F_y$  and  $F_z$  respectively.

All the performance of the three models are reported in table V.

#### D. Dynamic validation

Although a k-fold cross validation has been performed to validate the non-linear regression models on the training data, it is worth verifying the prediction ability of the force while the FSD is subject to dynamic loading.

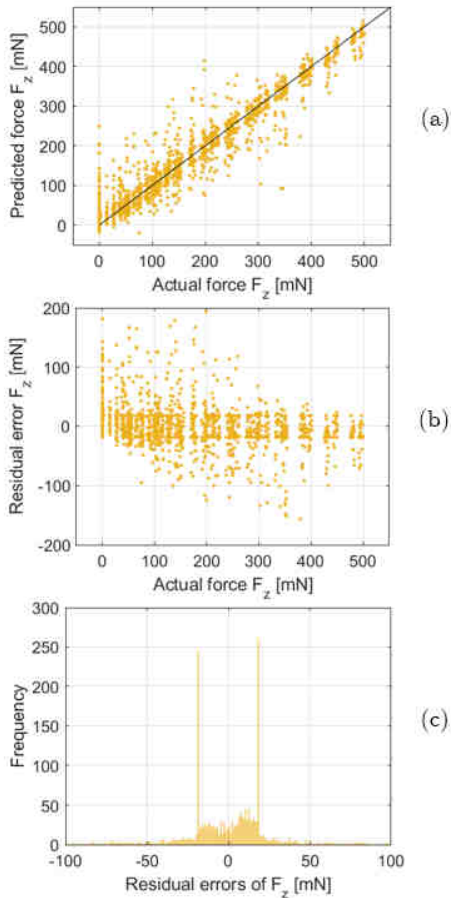


Fig. 12: The predicted axial force  $F_z$  versus the actual value using (a) support vector regression, (b) its residual error, and (c) the histogram of the residual error of  $F_z$ .

The protocol consists in orienting the prototype in several directions and randomly loading and unloading it against the scale while the readings of the interrogator and the scale are recorded on the same test bench described in figure 6. To be able to use the models, the directions chosen are in the range of the calibrated directions (known  $\alpha$ - $\beta$ ) as well as the range magnitude of the force applied. For that purpose, two testing data are generated. The first is made with the combination of directions  $0^\circ$ - $45^\circ$  and  $180^\circ$ - $15^\circ$  while the second is made with the combination of directions  $90^\circ$ - $15^\circ$  and  $90^\circ$ - $45^\circ$ . The choice of these angles allows that both data sets are alternatively canceling  $F_x$  and  $F_y$  to verify the ability of the models to correctly predict 0 values.

In figure 13 (a), the predicted values of  $F_x$  are closely following the actual values measured during the validation test. The global RMSE obtained for the prediction of  $F_x$  is 34.5 mN with  $R^2$  equal to 0.96 which is consistent with the performance of the model on the training data. The mean residual error is equal to 0.05 +/- 34.6 mN. As for the prediction of  $F_y$  in figure 13 (b), the RMSE is 7.6 mN. One can observe that the predicted values are close to the actual ones. The calculated mean residual error is equal to 3.5 +/- 9.3 mN. The results are acceptable. The NN model along Y-direction is able to

Force	Range [mN]	RMSE	$R^2$	Accuracy	Resolution
$F_x$	[-500 ; 500]	29.8 mN 2.9% of f.s.	0.96	0.04 +/- 20.3 mN	5.3 mN
$F_y$	[-500 ; 500]	23 mN 2.3% of f.s.	0.98	0.05 +/- 13.4 mN	5.4 mN
$F_z$	[0 ; 500]	49.9 mN 9.9% of f.s.	0.87	2.2 +/- 37 mN	2.9 mN

TABLE V: Summary of the performance of the models trained to predict  $F_x$ ,  $F_y$  and  $F_z$ . The values reported are computed when the models are applied to the training data and validated by 5 folds cross validation. The mean residual errors are taken as a measure of accuracy.

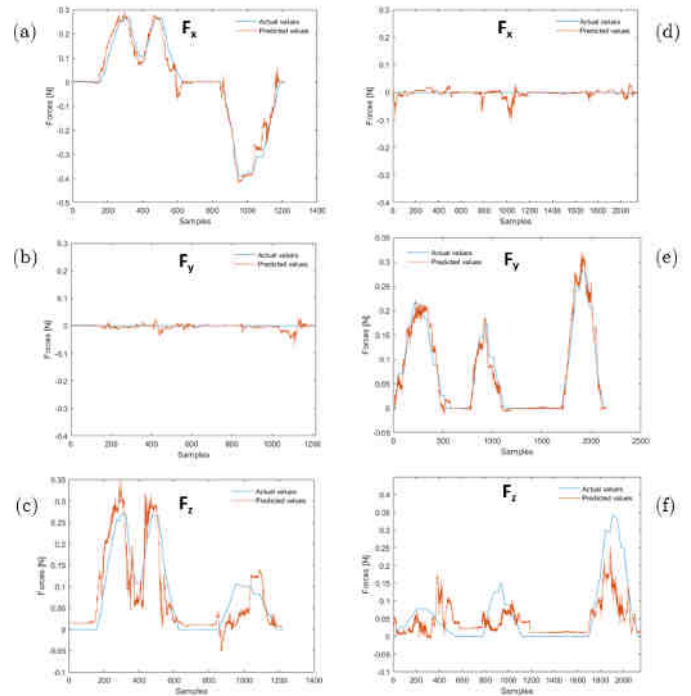


Fig. 13: (a)-(c) : Prediction of  $F_x$ ,  $F_y$  and  $F_z$  when  $\alpha$ - $\beta$  ranged from  $0^\circ$ - $45^\circ$  to  $180^\circ$ - $15^\circ$ . (d)-(f) : Prediction of  $F_x$ ,  $F_y$  and  $F_z$  when  $\alpha$ - $\beta$  ranged from  $90^\circ$ - $15^\circ$  to  $90^\circ$ - $45^\circ$ .

correctly predict zero values of  $F_y$  and thus decouple the transverse forces. As expected after analyzing the performance of the SVR model on the training data, the prediction of  $F_z$  is less efficient than the transverse forces  $F_x$  and  $F_y$  even in testing data. The global RMSE is equal to 47.2 mN with  $R^2$  worth 0.71. These results can be observed in figure 13 (c) where there is a poorer superposition of predicted and actual force values. The mean residual error is equal to 0.9 +/- 47.3 mN.

The prediction of  $F_x$  illustrated in figure 13 (d) showed a RMSE of 23.4 mN which is higher than the RMSE calculated for  $F_y$  (7.6 mN) when it was supposed to be equal to 0. One can conclude that the NN model computing  $F_y$  is better to predict zero values than the NN model related to  $F_x$ . However, even if the RMSE is higher than expected, the mean residual

error is equal to 3.4 +/- 13.5 mN. The prediction of  $F_y$  in the second testing data set is excellent. The superposition of predicted and actual values is very close (see figure 13 (e)). The RMSE obtained is 17.7 mN with  $R^2$  equal to 0.96. The mean error is equal to 0.2 +/- 17.8 mN. Finally, the computation of  $F_z$  in this last configuration provided a RMSE equal to 66.7 mN with  $R^2$  worth 0.42 which indicates a poor superposition of predicted versus actual force values as it is observed in figure 13 (f). The mean error is 15.7 +/- 64.9 mN. Comparatively to the prediction of  $F_z$  in the first testing condition, here the results are less qualitative.

## V. DISCUSSION

### A. General performance

For comparable dimensions and force range, the FSD shows resolution values in both lateral and axial directions that are in the same order of magnitude as those reported in the literature [20], [22], [32], which is satisfying knowing the effects due to the use of soft polymer as substrate for the FBGs. Although a more rigid notched structure could bring some functionalities to reduce the crosstalk errors of the force components, it also has the consequence of complicating the design and increasing the risk of fracture. In addition, the use of high-frequency current for ESD applications implies a preference for non-metallic material to prevent possible current leakage, which is completely avoided by using soft polymer. The force prediction performance in terms of RMSE is also comparable to similar FBG based force sensors with less than 2.9% error on full scale for lateral forces ( $F_x$  and  $F_y$ ) [21], [22]. However, the RMSE of axial force prediction is slightly less than 10%, which is higher than some previous studies [21], [32], but using only 3 FBGs instead of 4. In this case, the performance is comparable to the existing metallic FBG-based force sensor [22]. This work has thus provided a successful FBG-based force sensor for a flexible soft polymer catheter without the need for a notched metallic complex structure. Most importantly, the sensor shows good consistency with reliable repeatability under laboratory conditions. Further work should be carried out to evaluate this consistency in a humid and thermally varying environment, i.e. a GI tract. However, the use of a data-driven approach to model the force prediction capability of the sensor helps to capture the intrinsic non-linearities and hysteresis that occur during calibration and provide the satisfactory results in dynamic validation. Increasing the number of calibrated directions could improve the consistency of the sensor in real-world conditions.

### B. Temperature compensation

Temperature has been neglected in these experiments, since all the tests have been carried out in a stable thermal environment, although slight temperature perturbations could have an effect on the measurements, especially in the force range chosen in this work, as it has been reported previously [30]. However, an active method to compensate for temperature influence on force measurements has to be implemented since endoscopic submucosal dissection is a heat producing

procedure that will definitely impact the FBGs sensitivities [36].

Several means can be considered for that purpose including the use of chirped and tapered FBGs [37], [38], dual-wavelength FBGs [41], in-fiber Bragg gratings [42] or an extra unstrained reference FBG [39]. The latter has been investigated in an endoscopic device in [40] and appears to be the most promising. This method is most likely to be implemented in the next iteration of the FSD to compensate for temperature.

### C. Material and assembly

The use of soft material as a substrate for the nitinol tubes and the FBGs had a direct impact on the calibration data by showing viscoelastic effects and non-linearities. The choice of more rigid material could solve this issue but is still not sufficient since conventional catheter are made soft to maintain flexibility to move according to the endoscope in the GI tract. Using other types of adhesives like epoxy [43] with lower viscoelastic effects could also substantially increase quality of the force measurements.

Improvements can be achieved also in the prototyping process since it is currently made manually which is prone to human error inducing a low accuracy of the assembly. In particular, the level of precision is limited when placing the FBGs inside the nitinol tubes which can lead to misalignment that could explain the lower results of the prediction of  $F_z$  under axial loads. However, the use of a data driven approach has limited the uncertainty of the assembly but further work still has to be conducted in this regard.

### D. Versatility

Although this 3 DOF force sensing catheter has been developed for the purpose of acquiring force information during ESD, its design allows to explore other endoscopic applications since the central lumen can host other tools than an electrosurgical knife. Actually, this force sensing device can be intended for tissue palpation, needle injection or elastography.

## VI. CONCLUSION

A 3 DOF force sensing device (FSD) has been designed and implemented for the application of endoscopic submucosal dissection. This is the first flexible catheter made of soft polymer implementing FBGs for 3 DOF force sensing to the knowledge of the author. The challenge to embed several FBGs into a device with endoscopic dimensions (diameter less than 2.8 mm) while allowing the space for an electrosurgical wire as the principal tool was successfully achieved. A minimalist design has been implemented requiring 3 FBGs placed inside of nitinol tubes circumferentially to the section of a catheter. A force calibration test bench was specifically designed to calibrate the FSD in 30 3D spatial directions that cover most of its use cases. The challenge of tackling the non-linearities between the wavelength shifts and the forces applied on the tip of the catheter, due to prototyping imprecision and presence of viscoelastic material such as the soft polymer

which the catheter is made of and adhesive, was managed by the implementation of non-linear regression models. A hybrid model made of mono- and bi-layered neural networks for the prediction of  $F_x$  and  $F_y$  and a support vector regression for the prediction of  $F_z$  was built and validated with k-fold cross validation. The device is able to measure forces in the range of [-500 ; 500 ] mN for transverse forces and [0 ; 500] mN for axial force. RMSE along X- and Y-directions are equal to 29.8 mN and 23 mN respectively representing less than 3% of the full scale while RMSE along Z-direction is equal to 49.9 mN which is less than 10% of the full scale. These models were also verified in dynamic conditions. The results are promising and satisfying all the technical requirements. Further work should implement a robust temperature compensation technique in order to validate the 3 DOF force sensor in ex-vivo animal settings during ESD procedure. For that purpose, an automation of the calibration bench is necessary to avoid human error during the process, reduce its duration and enhance its repeatability from one device to another. Finally, a force-feedback visual interface will also be designed and integrated to the force sensing device.

## REFERENCES

- [1] Kuipers, E. & Haringsma, J. Diagnostic and therapeutic endoscopy. *Journal Of Surgical Oncology*. **92**, 203-209 (2005)
- [2] Van der Wiel, S., Küttner Magalhães, R., Rocha Gonçalves, C., Dinis-Ribeiro, M., Bruno, M. & Koch, A. Simulator training in gastrointestinal endoscopy – From basic training to advanced endoscopic procedures. *Best Practice And Research Clinical Gastroenterology*. **30**, 375-387 (2016)
- [3] Yamamoto, H. Endoscopic submucosal dissection-current success and future directions. *Nature Reviews Gastroenterology And Hepatology*. **9**, 519-529 (2012)
- [4] Gate, C. Endoscopic therapy for gastric neoplasms. (<https://clinicalgate.com/endoscopic-therapy-for-gastric-neoplasms/>), (Accessed: 24 May 2023)
- [5] Ko Young Bo Unexpected Delayed Colon Perforation after the Endoscopic Submucosal Dissection with Snaring of a Laterally Spreading Tumor. *Clin Endosc*. **48**, 570-575 (2015)
- [6] Kakushima, N. & Fujishiro, M. Endoscopic submucosal dissection for gastrointestinal neoplasms. *World Journal Of Gastroenterology*. **14**, 2962-2967 (2008)
- [7] Draganov, P. Advances in endoscopy.. *Gastroenterology & Hepatology*. **14**, 50-52 (2018)
- [8] Pimentel-Nunes, P. et al. Endoscopic submucosal dissection: European Society of Gastrointestinal Endoscopy (ESGE) Guideline. *Endoscopy*. **47**, 829-854 (2015)
- [9] Wang, A. & Draganov, P. Training in endoscopic submucosal dissection from a Western perspective. *Techniques In Gastrointestinal Endoscopy*. **19**, 159-169 (2017)
- [10] Vrieliink, T., Zhao, M., Darzi, A. & Mylonas, G. ESD CYCLOPS: A New Robotic Surgical System for GI Surgery. *2018 IEEE International Conference On Robotics And Automation (ICRA)*. (2018,5)
- [11] Ge, P., Thompson, C., Jirapinyo, P. & Aihara, H. Suture pulley countertraction method reduces procedure time and technical demand of endoscopic submucosal dissection among novice endoscopists learning endoscopic submucosal dissection: a prospective randomized ex vivo study. *Gastrointestinal Endoscopy*. **89**, 177-184 (2019,1)
- [12] Matsuzaki, I., Hattori, M., Hirose, K., Esaki, M., Yoshikawa, M., Yokoi, T., Kobayashi, M., Miyahara, R., Hirooka, Y. & Goto, H. Magnetic anchor-guided endoscopic submucosal dissection for gastric lesions (with video). *Gastrointestinal Endoscopy*. **87**, 1576-1580 (2018,6)
- [13] Matsuzaki, I., Hattori, M., Yamauchi, H., Goto, N., Iwata, Y., Yokoi, T., Tsunemi, M., Kobayashi, M., Yamamura, T. & Miyahara, R. Magnetic anchor-guided endoscopic submucosal dissection for colorectal tumors (with video). *Surgical Endoscopy*. **34**, 1012-1018 (2019,9)
- [14] Kume, K. Flexible robotic endoscopy: current and original devices. *Computer Assisted Surgery*. **21**, 150-159 (2016,1)
- [15] Yeung, B. Application of robotics in gastrointestinal endoscopy: A review. *World Journal Of Gastroenterology*. **22**, 1811 (2016)
- [16] Iwasa, T., Nakadate, R., Onogi, S., Okamoto, Y., Arata, J., Oguri, S., Ogino, H., Ihara, E., Ohuchida, K., Akahoshi, T., Ikeda, T., Ogawa, Y. & Hashizume, M. A new robotic-assisted flexible endoscope with single-hand control: endoscopic submucosal dissection in the ex vivo porcine stomach. *Surgical Endoscopy*. **32**, 3386-3392 (2018,4)
- [17] Sivananthan, A., Glover, B., Ayaru, L., Patel, K., Darzi, A. & Patel, N. The evolution of lower gastrointestinal endoscopy: where are we now?. *Therapeutic Advances In Gastrointestinal Endoscopy*. **13** pp. 263177452097959 (2020,1)
- [18] Li, W., Shen, M., Gao, A., Yang, G. & Lo, B. Towards a Snake-Like Flexible Robot for Endoscopic Submucosal Dissection. *IEEE Transactions On Medical Robotics And Bionics*. **3**, 257-260 (2021,2), <https://doi.org/10.1109/tmr.2020.3045507>
- [19] Tosi, D., Schena, E., Molardi, C. & Korganbayev, S. Fiber optic sensors for sub-centimeter spatially resolved measurements: Review and biomedical applications. *Optical Fiber Technology*. **43** pp. 6-19 (2018)
- [20] Li, T., Shi, C. & Ren, H. Three-Dimensional Catheter Distal Force Sensing for Cardiac Ablation Based on Fiber Bragg Grating. *IEEE/ASME Transactions On Mechatronics*. **23** pp. 2316-2327 (2018,10)
- [21] Deng, Y., Yang, T., Dai, S. & Song, G. A Miniature Triaxial Fiber Optic Force Sensor for Flexible Ureteroscopy. *IEEE Transactions On Biomedical Engineering*. **68**, 2339-2347 (2021,8)
- [22] Ping, Z., Zhang, T., Gong, L., Zhang, C. & Zuo, S. Miniature Flexible Instrument with Fibre Bragg Grating-Based Triaxial Force Sensing for Intraoperative Gastric Endomicroscopy. *Annals Of Biomedical Engineering*. **49**, 2323-2336 (2021,4)
- [23] Lai, W., Cao, L., Liu, J., Tjin, S. & Phee, S. A Three-Axial Force Sensor Based on Fiber Bragg Gratings for Surgical Robots. *IEEE/ASME Transactions On Mechatronics*. **27**, 777-789 (2022,4)
- [24] Dogramadzi, S., Virk, G., Bell, G., Rowland, R. & Hancock, J. Recording forces exerted on the bowel wall during colonoscopy: in vitro evaluation. *The International Journal Of Medical Robotics And Computer Assisted Surgery*. **1**, 89-97 (2005,12)
- [25] Shi, C., Li, M., Lv, C., Li, J. & Wang, S. A High-Sensitivity Fiber Bragg Grating-Based Distal Force Sensor for Laparoscopic Surgery. *IEEE Sensors Journal*. **20**, 2467-2475 (2020)
- [26] Lv, C., Wang, S. & Shi, C. A High-Precision and Miniature Fiber Bragg Grating-Based Force Sensor for Tissue Palpation During Minimally Invasive Surgery. *Annals Of Biomedical Engineering*. **48**, 669-681 (2020)
- [27] Kang, D., Park, S., Hong, C. & Kim, C. The signal characteristics of reflected spectra of fiber Bragg grating sensors with strain gradients and grating lengths. *NDT & E International*. **38**, 712-718 (2005,12)
- [28] Xiong, L., Jiang, G., Guo, Y. & Liu, H. A Three-Dimensional Fiber Bragg Grating Force Sensor for Robot. *IEEE Sensors Journal*. **18** pp. 3632-3639 (2018)
- [29] Zhang, J. & Li, Y. Calibration method for fiber bragg grating temperature sensor. *2009 9th International Conference On Electronic Measurement Instruments*. pp. 2822-2825 (2009)
- [30] Gao, A., Liu, N., Zhang, H., Wu, Z. & Yang, G. Spiral FBG sensors-based contact detection for confocal laser endomicroscopy. *Biosensors And Bioelectronics*. **170** pp. 112653 (2020)
- [31] He, X., Handa, J., Gehlbach, P., Taylor, R. & Iordachita, I. A sub-millimetric 3-DOF force sensing instrument with integrated fiber bragg grating for retinal microsurgery. *IEEE Transactions On Biomedical Engineering*. **61**, 522-534 (2014)
- [32] Gao, A., Zhou, Y., Cao, L., Wang, Z. & Liu, H. Fiber Bragg Grating-Based Triaxial Force Sensor With Parallel Flexure Hinges. *IEEE Transactions On Industrial Electronics*. **65**, 8215-8223 (2018)
- [33] Wu, Z., Gao, A., Liu, N., Jin, Z. & Yang, G. FBG-Based Triaxial Force Sensor Integrated with an Eccentrically Configured Imaging Probe for Endoluminal Optical Biopsy. *2020 IEEE International Conference On Robotics And Automation (ICRA)*. pp. 1625-1631 (2020)
- [34] Choi, H., Lim, Y. & Kim, J. Three-axis force sensor with fiber Bragg grating. *2017 39th Annual International Conference Of The IEEE Engineering In Medicine And Biology Society (EMBC)*. pp. 3940-3943 (2017)
- [35] Clinic, C. A minimally invasive treatment for early GI cancers. (<https://consultqd.clevelandclinic.org/a-minimally-invasive-treatment-for-early-gi-cancers/>), (Accessed: 09 March 2023)
- [36] Ben Hassen, R., Caucheteur, C. & Delchambre, A. FBGs temperature sensor for electrosurgical knife subject to high voltage and high-frequency current. *Optical Sensing And Detection VI*. **11354** pp. 291 - 298 (2020)

- [37] Xu, M., Tucknott, J., Reekie, L., Dong, L. & Cruz, J. Temperature-independent strain sensor using a chirped Bragg grating in a tapered optical fibre. *Electronics Letters*. **31**, 823-825 (1995,5)
- [38] Abushagur, A., Arsal, N., Elgaud, M. & Bakar, A. Development of a 1-DOF Force Sensor Prototype Incorporating Tapered Fiber Bragg Grating for Microsurgical Instruments. *IEEE Access*. **7** pp. 168520-168526 (2019)
- [39] Zhou, Z. & Ou, J. Techniques of temperature compensation for FBG strain sensors used in long-term structural monitoring. *Fundamental Problems Of Optoelectronics And Microelectronics II*. **5851** pp. 167 - 172 (2005)
- [40] Ben Hassen, R. Design and Development of a 3 DOF Force Sensor Using Fiber Bragg Gratings in Endoscopic Applications. (Université libre de Bruxelles, 2023), PhD thesis
- [41] Xu, M., Reekie, L., Dakin, J. & Archambault, J. Discrimination between strain and temperature effects using dual-wavelength fibre grating sensors. *Electronics Letters*. **30**, 1085-1087 (1994,6)
- [42] James, S., Dockney, M. & Tatum, R. Simultaneous independent temperature and strain measurement using in-fibre Bragg grating sensors. *Electronics Letters*. **32**, 1133 (1996), <https://doi.org/10.1049/el:19960732>
- [43] Lai, W., Cao, L., Tan, R., Phan, P., Hao, J., Tjin, S. & Phee, S. Force Sensing With 1 mm Fiber Bragg Gratings for Flexible Endoscopic Surgical Robots. *IEEE/ASME Transactions On Mechatronics*. **25**, 371-382 (2020)



**Alain Delchambre** has obtained his M.S. and Ph.D. degrees in Mechanical engineering from the University of Brussels (ULB, Belgium) respectively in 1983 and 1990.

After three years in industry, he joined a research center for the Belgian Metalworking Industry. Since 1994, he is Professor at the Faculty of Engineering in ULB. He was Dean of the Faculty (2006-2010) and Chairman of the Board of the University (2011-2014). He is director of the Bio-, Electro- and Mechanical- Systems department (BEAMS). He has published three books and more than 100 papers in the area of concurrent engineering, computer aided design and design of medical devices. He has created 4 spin-off companies involved in medical technologies.



**Ramzi Ben Hassen** received his M.S. and Ph.D. degrees in biomedical engineering from University of Brussels (ULB, Belgium) in 2018 and 2023 respectively.

He is currently a Postdoctoral Researcher with the Bio, Electro and Mechanical Systems department (BEAMS), ULB, Belgium. He is working on developing force sensitive catheter for therapeutic endoscopy funded by the Michel Cremer Fondation. His research interests include smart catheters, medical devices and AI

applied in sensors.



**Arnaud Lemmers** received his M.D. degree in 2003 and his Ph.D. degree in 2009 before completing his certificate in gastroenterology in 2010.

He is currently a Professor at the Faculty of Medicine of the University of Brussels (ULB) and Director of the Endoscopy clinic (digestive endoscopy) at Erasme Hospital (Brussels, Belgium). He is an expert on general gastroenterology with a special focus in gastrointestinal endoscopy and tumor resection through advanced

techniques (EMR and ESD). He is, among others, President of the Belgian Society of Gastrointestinal Endoscopy (BSGIE) and Member of the European Society of Gastrointestinal Endoscopy (ESGE) since 2021 and 2011 respectively. He regularly collaborates with engineers in the development of medical devices.